Suppression of STING Associated with LKB1 Loss in KRAS-Driven Lung Cancer

Shunsuke Kitajima[1], Elena Ivanova[1,2], Sujuan Guo[1,2], Ryohei Yoshida[1], Marco Campisi[1,3,4], Shriram K. Sundararaman[1,5], Shoichiro Tange[6], Yoichiro Mitsuishi[7], Tran C. Thai[1], Sayuri Masuda[8], Brandon P. Piel[1], Lynette M. Sholl[9], Paul T. Kirschmeier[1,2], Cloud P. Paweletz[1,2], Hideo Watanabe[10], Mamiko Yajima[11], and David A. Barbie[1]

ABSTRACT

KRAS-driven lung cancers frequently inactivate *TP53* and/or *STK11/LKB1*, defining tumor subclasses with emerging clinical relevance. Specifically, *KRAS-LKB1* (KL)–mutant lung cancers are particularly aggressive, lack PD-L1, and respond poorly to immune checkpoint blockade (ICB). The mechanistic basis for this impaired immunogenicity, despite the overall high mutational load of *KRAS*-mutant lung cancers, remains obscure. Here, we report that LKB1 loss results in marked silencing of stimulator of interferon genes (STING) expression and insensitivity to cytoplasmic double-strand DNA (dsDNA) sensing. This effect is mediated at least in part by hyperactivation of DNMT1 and EZH2 activity related to elevated S-adenylmethionine levels and reinforced by DNMT1 upregulation. Ectopic expression of STING in KL cells engages IRF3 and STAT1 signaling downstream of TBK1 and impairs cellular fitness, due to the pathologic accumulation of cytoplasmic mitochondrial dsDNA associated with mitochondrial dysfunction. Thus, silencing of STING avoids these negative consequences of LKB1 inactivation, while facilitating immune escape.

SIGNIFICANCE: Oncogenic *KRAS*-mutant lung cancers remain treatment-refractory and are resistant to ICB in the setting of LKB1 loss. These results begin to uncover the key underlying mechanism and identify strategies to restore STING expression, with important therapeutic implications because mitochondrial dysfunction is an obligate component of this tumor subtype.

See related commentary by Corte and Byers, p. 16.

[1]Department of Medical Oncology, Dana-Farber Cancer Institute, Boston, Massachusetts. [2]Belfer Center for Applied Cancer Science, Dana-Farber Cancer Institute, Boston, Massachusetts. [3]Department of Mechanical Engineering, Massachusetts Institute of Technology, Cambridge, Massachusetts. [4]Department of Mechanical and Aerospace Engineering, Politecnico di Torino, Turin, Italy. [5]University of Virginia School of Medicine, University of Virginia, Charlottesville, Virginia. [6]Department of Human Genetics, Graduate School of Biomedical Science, Tokushima University, Tokushima, Japan. [7]Department of Respiratory Medicine, Graduate School of Medicine, Juntendo University, Tokyo, Japan. [8]Department of Pediatric Oncology, Dana-Farber Cancer Institute, Boston, Massachusetts. [9]Department of Pathology, Brigham and Women's Hospital, Boston, Massachusetts. [10]Tisch Cancer Institute, Icahn School of Medicine at Mount Sinai, New York, New York. [11]MCB Department, Brown University, Providence, Rhode Island.

Note: Supplementary data for this article are available at Cancer Discovery Online (http://cancerdiscovery.aacrjournals.org/).

Corresponding Author: David A. Barbie, Dana-Farber Cancer Institute, 450 Brookline Avenue LC4115, Boston, MA 02215. Phone: 617-632-6049; Fax: 617-394-2876; E-mail: dbarbie@partners.org

doi: 10.1158/2159-8290.CD-18-0689

INTRODUCTION

KRAS-mutant non–small cell lung cancers (NSCLC) inactivate specific tumor suppressors that differentially affect the tumor-immune microenvironment (1, 2). In particular, although *KRAS-TP53* (KP) lung tumors engage the PD-1/PD-L1 immune checkpoint, *KRAS-LKB1* (KL) tumors lack PD-L1 expression and fail to respond to immune checkpoint blockade (ICB; ref. 3). KL tumors also preferentially secrete certain cytokines/chemokines such as IL6, which promotes an immunosuppressive phenotype associated with myeloid cell recruitment (1); however, the underlying molecular basis for this altered innate immune response remains obscure.

LKB1 is the major upstream activator of AMPK, an energy sensor activated in the setting of low ATP concentrations, inhibiting mTORC1. AMPK also targets defective mitochondria for autophagy (4). Thus, in the absence of LKB1, *KRAS*-mutant lung cancers not only develop a growth advantage due to unrestrained mTOR signaling, but also develop mitochondrial dysfunction (5). LKB1 inactivation creates additional metabolic consequences, including increased serine utilization and synthesis of S-adenylmethionine (SAM; ref. 6). Because SAM is a substrate for multiple epigenetic silencing enzymes such as DNMT1 and EZH2, this facilitates plasticity of LKB1 cells to undergo transcriptional adaptation to a variety of stresses. AMPK also directly phosphorylates and inhibits EZH2, further contributing to heightened EZH2 activity following LKB1 loss (7).

Stimulator of interferon genes (STING; encoded by *TMEM173*) has emerged as a key regulator of the innate immune response and as a target for cancer immunotherapy (8). Aberrant cytoplasmic double-strand DNA (dsDNA) is detected by cyclic GMP–AMP synthase (cGAS), which produces the second messenger cGAMP that directly activates STING and promotes its cellular relocalization. Activated STING binds to TBK1, a critical downstream regulator of innate immune signaling, and bridges it to IRF3, thereby inducing expression of cytotoxic type 1 IFNs and chemokines such as CXCL10 that facilitate T-cell recruitment. Notably, TBK1 also activates NF-κB signaling and, together with its homolog IKKε, preferentially engages this prosurvival effector arm of the innate immune response in *KRAS*-mutant lung cancers (2). TBK1/IKKε-induced cytokines/chemokines such as IL6 and CCL5 can promote tumorigenesis (9) and create an immunosuppressive microenvironment that impairs response to PD-1/PD-L1 ICB (10).

Although STING signaling evolved as an innate immune mechanism to defend against viral and other pathogens, it has become increasingly apparent that STING is frequently activated due to multiple other defects that result in accumulation of cytoplasmic dsDNA (8). In addition to cytoplasmic leakage or failed clearance of nuclear dsDNA, sensing of cytosolic mitochondrial (mt) dsDNA has emerged as an important activator of the cGAS–STING pathway. For example, apoptotic caspases, which are also released from mitochondria but tightly regulated, serve a recently recognized function to eliminate the dying cell and avoid this aberrant innate immune sensing of mtDNA (11). In the context of cancer, aberrant sensing of mtDNA by STING may have important consequences for tumor biology. Indeed, here we uncover a novel mechanism whereby KL tumor cells epigenetically silence STING to avoid the deleterious effects of sensing cytosolic mtDNA.

RESULTS

LKB1 Modulates STING Expression in *KRAS*-Mutant Lung Cancer

To identify robust gene expression signatures enriched specifically in KL relative to KP cancer cells, we integrated lung data from The Cancer Genome Atlas (TCGA) with the Cancer Cell Line Encyclopedia (CCLE) and performed gene set enrichment analysis (GSEA). As expected, this analysis revealed KL-specific upregulation of signatures associated with oxidative stress (q value < 0.001), consistent with the known mitochondrial dysfunction associated with LKB1 inactivation (ref. 5; Fig. 1A; Supplementary Fig. S1A). In contrast, type I IFN signaling (q value < 0.001) was among the most significantly downregulated pathway signatures in KL cells (Fig. 1A; Supplementary Fig. S1A). Because cell-autonomous type I IFN responses are typically regulated by dsDNA or dsRNA sensing pathways, we next examined differential expression of genes along these signaling axes (Fig. 1B). This identified KL-specific downregulation of genes involved in dsDNA sensing, especially *TMEM173/STING* (Fig. 1C), which was also reduced in LKB1-mutant *KRAS* wild-type (WT) NSCLC cell lines (Fig. 1C; Supplementary Fig. S1B). To validate this finding, we used IHC to analyze tumor cell–specific STING protein levels across a panel of 64 patient-derived NSCLC samples enriched for *KRAS*-mutated status. LKB1 loss was robustly associated with either complete absence of or significant reduction in STING levels in tumor cells (P < 0.0001; Fig. 1D; Supplementary Fig. S1C). Together, these data confirmed that LKB1 inactivation is associated with suppression of STING in *KRAS*-mutant lung cancer.

To investigate this finding further, we next examined STING expression across a panel of KL versus KP lung cancer cell lines. STING protein levels were either significantly downregulated (H1944, H2122, and H1355 cells—STING^{lo}) or completely undetectable (A549, A427, and H23 cells—STING^{absent}) in KL cell lines, regardless of p53 comutation (Fig. 1E). In contrast, levels of cGAS, which directly binds cytoplasmic dsDNA and is upstream of STING, were maintained in KL cells (Supplementary Fig. S1D). The relationship between STING downregulation and LKB1 loss was observed even in *KRAS* WT cancer cell lines (Supplementary Fig. S1E). *STING* mRNA levels measured by qRT-PCR were also significantly downregulated in KL cells (Fig. 1F). Furthermore, treatment of KL cells with MG132 or bafilomycin failed to increase STING protein levels, arguing against enhanced proteasomal or autophagy-mediated degradation (Supplementary Fig. S1F), and consistent with regulation at the transcriptional level.

We next assessed the causal relationship between LKB1-AMPK signaling and regulation of STING expression. CRISPR/Cas9-mediated deletion of *LKB1* or inhibition of downstream AMPK activity in KP cell lines (H2009, H441, and H358) decreased STING levels (Fig. 1G; Supplementary Fig. S1G). Conversely, stimulation of AMPK activity by phenformin treatment further increased STING levels in KP cells

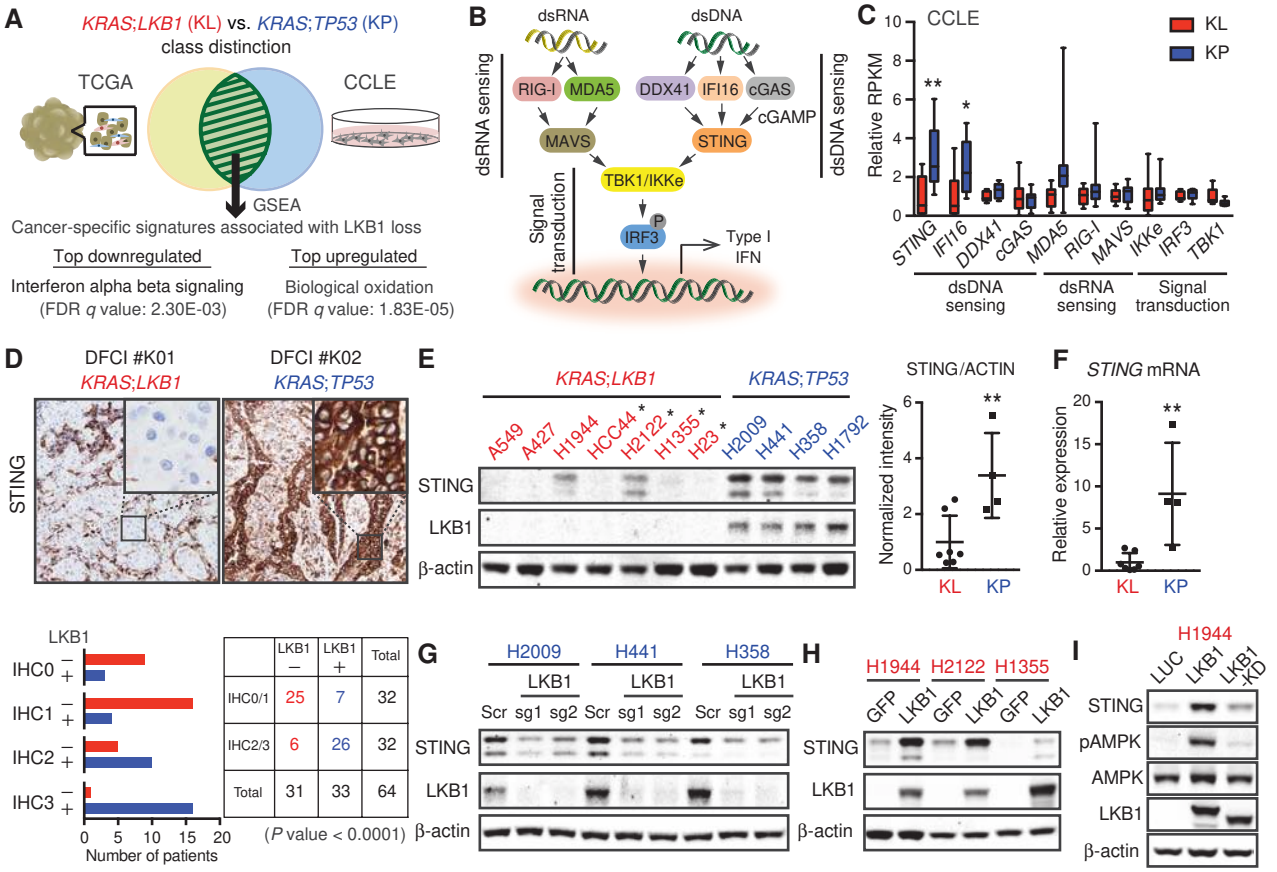

Figure 1. LKB1 modulates STING expression in *KRAS*-mutant lung cancer. **A,** Venn diagram showing differentially expressed genes between KL and KP in TCGA and CCLE. Top-ranked gene signatures derived from differentially expressed genes are represented. **B,** Schematic of dsRNA and dsDNA sensing pathways that induce type 1 IFN. **C,** Relative RPKM values of genes related to these pathways in KL and KP cells from CCLE. **D,** Representative STING IHC images of primary KL and KP NSCLC samples (top plot). Insets highlight tumor cell STING expression. STING intensity in cancer cells was scored in a blinded manner (bottom plot) on a scale of 0 to 3. IHC0, no staining; IHC1, low staining; IHC2, moderate staining; and IHC3, high staining. **E,** Immunoblot (IB) of the indicated proteins in KL (red) or KP (blue) cells (left). KL cell lines with an asterisk contain p53 mutation. STING expression was quantified by ImageJ and normalized to β-actin (right). **F,** qRT-PCR of *STING* in KL or KP cells. Each point represents one cell line. **G,** IB of the indicated proteins in KP cells transduced with scramble or *LKB1* single-guide RNA (sgRNA). **H** and **I,** IB of the indicated proteins in KL cells transduced with the indicated vectors. *P* values were calculated by unpaired two-tailed Student *t* test (**C, E,** and **F**) or Fisher exact test (**D**). *, $P < 0.05$; **, $P < 0.01$.

(Supplementary Fig. S1H). Finally, LKB1 reconstitution in STING^{lo} KL cell lines rescued STING expression (Fig. 1H), which required LKB1 kinase activity and pAMPK restoration (Fig. 1I). Thus, LKB1 signaling directly regulates STING expression in *KRAS*-mutant NSCLC cells.

Hyperactivation of DNMT1 and EZH2 Suppresses STING Expression in *KRAS-LKB1*–Mutant Cells

We noted that STING^{absent} cells failed to reinduce *STING* mRNA or protein expression following LKB1 reconstitution (Fig. 2A; Supplementary Fig. S2A). We therefore explored whether DNMT1 (6) or other chromatin modifiers might be related to this phenomenon. Indeed, STING^{absent} KL cell lines uniquely exhibited high levels of DNMT1 expression (Fig. 2B; Supplementary Fig. S2B and S2C), which can silence the STING promoter (12). Indeed, DNA hypermethylation was uniquely concentrated in the *STING* promoter region in STING^{absent} KL cell lines from CCLE data and by direct immunoprecipitation of methylated DNA (Fig. 2C and D), and was reversed by treatment with the DNMT inhibitor decitabine (DAC; Supplementary Fig. S2D). Furthermore, we confirmed increased DNMT1 binding to the *STING* promoter region in STING^{absent} KL cell lines compared with STING^{lo} KL cell lines (Fig. 2E). DNMT1 levels were also elevated in *KRAS* WT;*LKB1*-mutated NSCLC cells with robust STING silencing (Supplementary Fig. S2E). These data suggested active epigenetic repression of STING in lung cancer cell lines lacking LKB1.

To assess the functional role of DNMT1 and other possible regulators of STING silencing, we next treated KL cell lines with a focused panel of small-molecule inhibitors targeting epigenetic modifiers. As expected, treatment with DAC preferentially reactivated STING mRNA expression in STING^{absent} KL cell lines (Fig. 2F; Supplementary Fig. S2F), confirming the causal relationship between *STING* promoter methylation and repression of its expression. DAC treatment further reversed resistance of these cell lines to LKB1 reconstitution, rescuing the ability of LKB1 to reinduce both STING protein

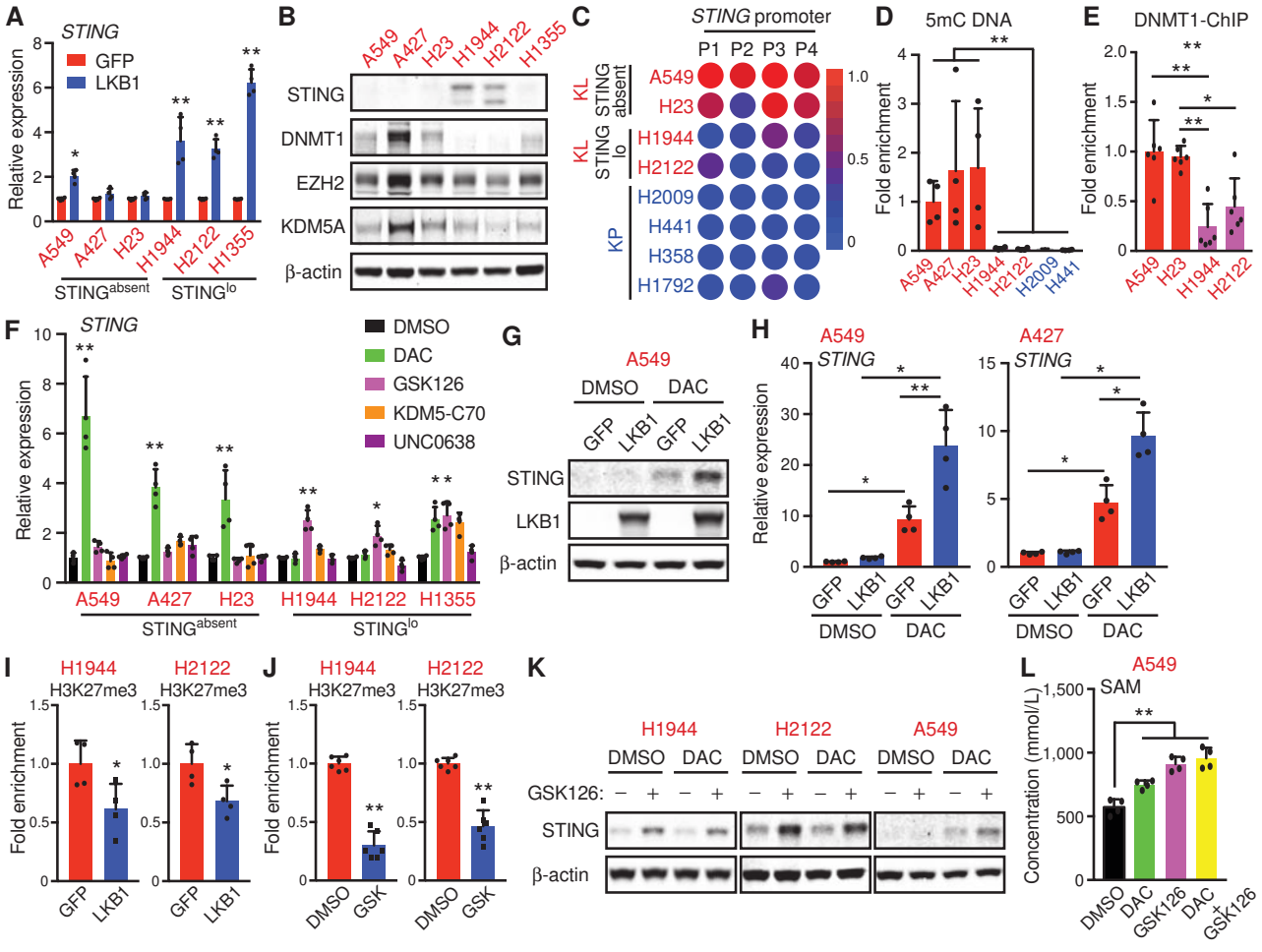

Figure 2. Hyperactivation of DNMT1 and EZH2 suppresses STING expression in KL cells. **A,** qRT-PCR of *STING* in KL cells transduced with GFP or LKB1. **B,** IB of the indicated proteins in KL cells. **C,** Dot plot heat maps showing DNA methylation levels in the STING promoter between KL and KP cells in CCLE (red = hypermethylation). The location of each position is as follows: P1, 5:138861649; P2, 5:138861807; P3, 5:138862442; and P4, 5:138862470. **D** and **E,** Levels of DNA methylation (**D**) or DNMT1 binding (**E**) within the 5′ UTR of *STING* (see Methods) normalized to input in KL cells. **F,** qRT-PCR of *STING* in KL cells treated with 100 nmol/L DAC, 5 μmol/L GSK126, 5 μmol/L KDM5-C70, or 500 nmol/L UNC0638 for 7 days. **G** and **H,** IB of the indicated proteins (**G**) or qRT-PCR of *STING* (**H**) in KL cells transduced with GFP or LKB1, and treated ± 100 nmol/L DAC for 7 days. **I** and **J,** H3K27me3 levels at 5′ UTR of *STING* normalized to the input in KL cells transduced with GFP or LKB1 (**I**) or treated with 5 μmol/L GSK126 for 7 days (**J**; $n = 4$ replicates from two independent experiments). **K,** IB of the indicated proteins in KL cells treated with 100 nmol/L DAC and/or 5 μmol/L GSK126 for 7 days. **L,** Measurement of SAM in A549 cells treated with 100 nmol/L DAC and/or 5 μmol/L GSK126 for 3 days ($n = 4$ replicates, representative of two independent experiments). *P* values were calculated by one-way (**E, F, H,** and **L**), two-way (**A**) ANOVA followed by Tukey *post hoc* test, or unpaired two-tailed Student *t* test (**D**, **I,** and **J**). *, $P < 0.05$; **, $P < 0.01$.

and mRNA expression (Fig. 2G and H). We noted that EZH2 inhibitor treatment (GSK126) also induced *STING* mRNA expression in STING^{lo} KL cells (Fig. 2F). We therefore examined levels of the H3K27Me3-repressive chromatin mark at the *STING* promoter and found that loss of LKB1 resulted in accumulation of H3K27Me3 levels (Fig. 2I). STING promoter H3K27Me3 levels were also specifically reduced by EZH2 inhibition (Fig. 2J). Thus, EZH2 inhibition alone was sufficient to augment STING protein levels in STING^{lo} KL cell lines and cooperated with DNMT1 inhibition to restore them in STING^{absent} KL cells (Fig. 2K). DAC, GSK126 treatment, and especially the combination also increased SAM levels in these cells (Fig. 2L), consistent with prior work (6). Indeed, we confirmed specific regulation of SAM levels by LKB1 in multiple KL cell lines (Supplementary Fig. S2G). Together, these data link heightened activity of both DNMT1 and EZH2, at least in part related to increased SAM availability, as mediators of STING repression in KL cells.

LKB1 Reconstitution Restores DNA Sensing and PD-L1 Expression in *KRAS-LKB1*–Mutant Cells

We next determined the impact of these findings on cytoplasmic dsDNA sensing. As expected, KP cells with intact STING retained activation of pTBK1 and pIRF3 following transfection with the dsDNA mimic poly (dA:dT), whereas this was abolished by STING deletion (Supplementary Fig. S3A). In contrast, KL cells were largely refractory to cytoplasmic dsDNA sensing, exhibiting minimal activation of pTBK1, pIRF3, or downstream pSTAT1 following poly (dA:dT) transfection (Fig. 3A; Supplementary Fig. S3A). As expected, LKB1

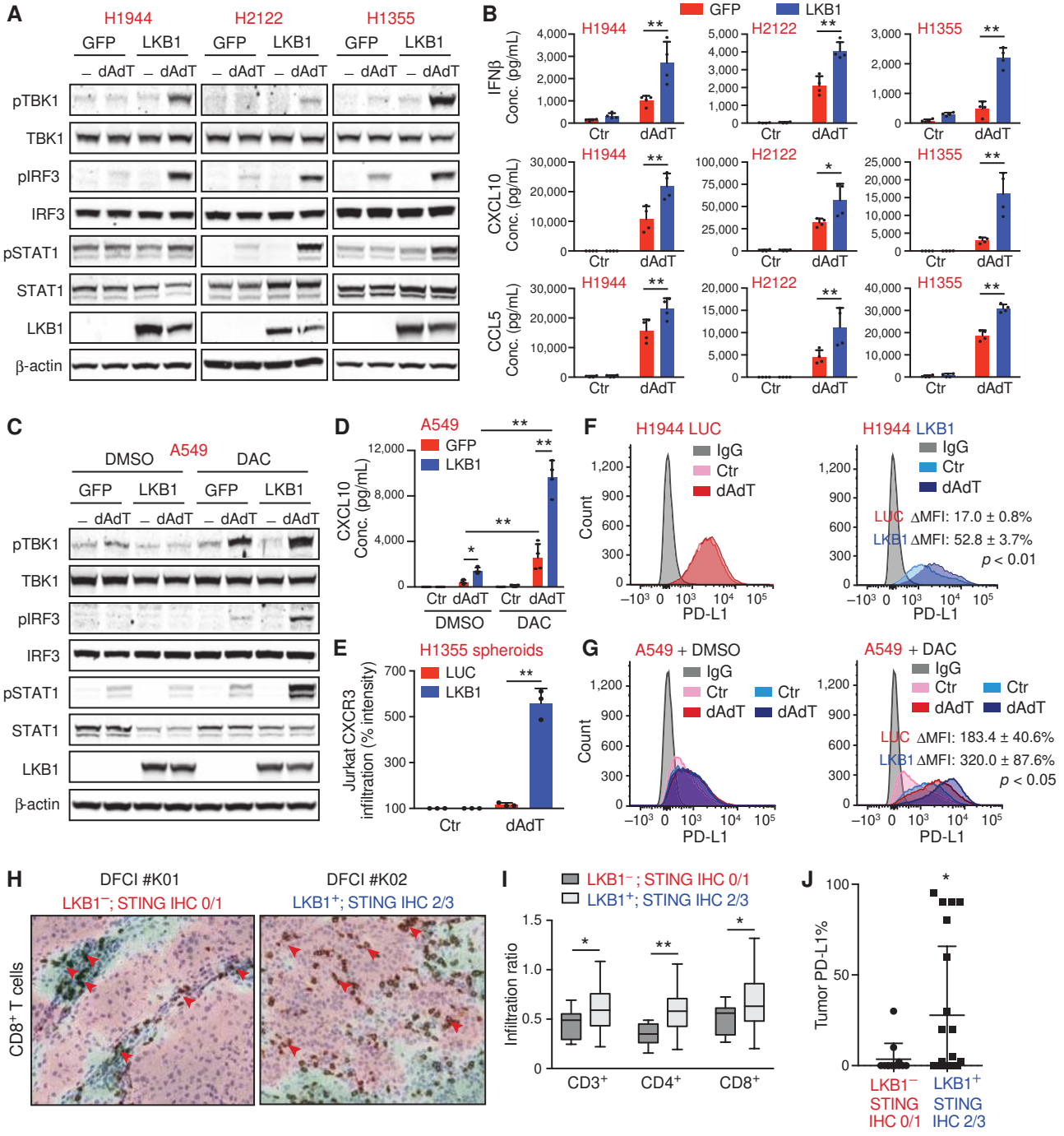

Figure 3. Defective sDNA sensing and impaired T-cell chemotaxis due to LKB1 inactivation. **A,** IB of the indicated proteins in KL cells transduced with GFP or LKB1, and treated ±1 μg/mL poly (dA:dT) for 4 hours. **B,** ELISA of human IFNβ, CXCL10, or CCL5 levels in conditioned medium (CM) derived from KL cells transduced with GFP or LKB1, and treated ±1 μg/mL poly (dA:dT) for 24 hours. **C,** IB of the indicated proteins in A549 cells transduced with GFP or LKB1, pretreated ±100 nmol/L DAC for 7 days, and treated ± 1 μg/mL poly (dA:dT) for 4 hours. **D,** ELISA of human CXCL10 levels in CM derived from A549 cells transduced with GFP or LKB1, pretreated ±100 nmol/L DAC for 7 days, and treated ±1 μg/mL poly (dA:dT) for 24 hours. **E,** Quantification of Jurkat CXCR3 infiltration into H1355 tumor spheroids (see Supplementary Fig. S3I and S3J). Values were normalized to each control. **F** and **G,** PD-L1 expression in H1944 cells transduced with NanoLuc or LKB1 (**F**), or A549 cells transduced with NanoLuc or LKB1, pretreated ±100 nmol/L DAC for 7 days (**G**), and treated ±125 ng/mL poly (dA:dT) for 12 hours. MFI, mean fluorescence intensity. ΔMFI, (dAdT-Ctr)/Ctr. Data are representative of three independent experiments. **H, I,** and **J,** IHC images and analysis from primary LKB1-negative; STING IHC 0/1 ($n = 12$) and LKB1-positive; STING IHC 2/3 NSCLC ($n = 22$) samples (see Fig. 1D). Red arrows highlight stained CD8⁺ T cells in both tumor epithelium (red) and stroma (green; **H**). PathAI (see Methods) was used to quantify CD3⁺/CD4⁺/CD8⁺ T-cell infiltration (**I**) and tumor PD-L1 expression (**J**). *P* values were calculated by two-way (**B, D,** and **E**) ANOVA followed by Tukey *post hoc* test, or unpaired two-tailed Student *t* test (**F, G, I,** and **J**). *, $P < 0.05$; **, $P < 0.01$.

reconstitution in STING^{lo} cell lines, which was sufficient to restore STING expression, rescued TBK1–IRF3 and STAT1 signal transduction downstream of dsDNA (Fig. 3A). This response was primarily specific to dsDNA sensing, because transfection with the dsRNA mimic poly (I:C) only marginally activated these pathways following LKB1 restoration (Supplementary Fig. S3B). LKB1 reconstitution in these cell lines also strongly enhanced dsDNA-induced secretion of the IRF3 targets IFNβ, CXCL10, and CCL5 by ELISA (Fig. 3B). Multiplexed cytokine/chemokine profiling further identified increased production of GM-CSF, CCL3, and IL1α following LKB1 reconstitution and poly (dA:dT) exposure, whereas IL6 was suppressed (Supplementary Fig. S3C), reflective of a broader shift between innate immune cytokine/chemokine production. As expected, STING^{absent} KL cells remained refractory to dsDNA sensing upon LKB1 reconstitution, consistent with the inability to reinduce STING; however, alleviation of DNMT1-mediated STING silencing by DAC treatment restored the capacity of LKB1 to enhance downstream signal transduction in response to dsDNA (Fig. 3C and D).

DAC treatment also enhanced the cytotoxicity of poly (dA:dT)–mediated STING agonism in A549 cells *in vitro* (Supplementary Fig. S3D). We therefore tested whether this combination could impair tumor formation in immunocompromised mice. Indeed, transient STING activation induced by poly (dA:dT) impaired tumorigenesis of A549 xenografts *in vivo*, which was significantly enhanced by DAC pretreatment (Supplementary Fig. S3E and S3F). Of note, we failed to observe tumor cell–specific penetration of currently available injectible STING agonists such as ADU-S100 even at very high concentrations (200 μmol/L; Supplementary Fig. S3G and S3H), precluding the ability to test the impact of DAC treatment on prolonged STING agonism *in vivo*.

We next explored the potential consequences of this defect in TBK1–IRF3–STAT1 signaling on the tumor immune microenvironment. Three-dimensional (3-D) microfluidic spheroid culture of isogenic LKB1 reconstituted STING^{lo} H1355 cells, which exhibited strong differential secretion of poly (dA:dT)–induced CXCL10 (Fig. 3B), and uncovered a direct relationship between LKB1 loss and defective recruitment of CXCR3-expressing Jurkat T cells (Fig. 3E; Supplementary Fig. S3I and S3J). Because PD-L1 expression is linked to downstream STAT1 signaling (13), we also tested whether defective dsDNA sensing links LKB1 loss with low PD-L1 levels. Indeed, LKB1 reconstitution restored poly (dA:dT)–induced PD-L1 surface expression in STING^{lo} KL cells (Fig. 3F), and in STING^{absent} KL cells together with DAC treatment (Fig. 3G). Consistent with these findings, IHC of patient-derived KRAS NSCLCs revealed a preferential decrease in intratumoral T-cell infiltration in STING/LKB1-negative specimens (Fig. 3H and I), and decreased PD-L1 levels (Fig. 3J). Thus, silencing of STING in KL cells directly contributes to impaired intratumoral T-cell recruitment and low PD-L1 expression.

STING Senses Pathologic Accumulation of mt dsDNA in *KRAS-LKB1*–Mutant Cells

We next sought to understand why active silencing of STING expression might occur in LKB1-mutant lung cancer cells. In contrast to KP cells, reintroduction of STING itself in multiple KL cell lines enhanced pTBK1, pIRF3, and pSTAT1 levels, as well as PD-L1 (Fig. 4A; Supplementary Fig. S4A). Downstream *CXCL10* expression was also preferentially induced following STING reconstitution in KL cells, and sensitive to the TBK1 inhibitor Compound 1 (ref. 10; Fig. 4B and C). Notably, STING-expressing KL cells grew more slowly compared with KP cell lines and exhibited increased apoptosis (Fig. 4D and E; Supplementary Fig. S4B–S4E). Because both IRF3 and downstream STAT1 signaling have antiviral cytotoxic functions, we cotreated cells with Compound 1 (TBK1i) or the JAK/STAT inhibitor ruxolitinib (ruxo) to assess the relative contributions of these pathways to STING-mediated apoptosis. Whereas TBK1 inhibition itself impaired viability of KL cells (14) yet partially reversed STING cytotoxicity, ruxo-mediated pSTAT1 inhibition strongly rescued STING-induced cell growth arrest and apoptosis (Fig. 4E and F; Supplementary Fig. S4F and S4G). These data suggest that downstream engagement of STAT1 signaling is the dominant contributor to STING-mediated tumor cell cytotoxicity in KL cells.

Because KL cells are characterized by impaired autophagy and mitochondrial dysfunction (ref. 5; Supplementary Fig. S4H), we wondered whether cytosolic release of dsDNA from defective mitochondria might underlie this intolerance of STING. Indeed, PicoGreen staining revealed that KL cell lines accumulated cytoplasmic DNA, in contrast to KP cells (Fig. 4G). Purification of mitochondria-free cytoplasmic fractions from KL versus KP cell lines and quantitative PCR confirmed preferential leakage of mt dsDNA in KL cells, as well as nuclear dsDNA in some cases (Fig. 4H; Supplementary Fig. S4I–S4K). Next, we utilized EtBr treatment (Rho 0) or sgPOLG expression to deplete mt DNA from KL cells, and successfully depleted the majority of cytoplasmic dsDNA from H2122 cells (Fig. 4I; Supplementary Fig. S4L–S4N). Multiplexed profiling of conditioned media revealed that CXCL10 and CCL5 were the most downregulated chemokines in STING-expressing Rho 0 and sg*POLG* H2122 cells compared with control lines (Fig. 4J; Supplementary Fig. S4O). STING-induced STAT1 activation was also prevented by mt DNA depletion (Fig. 4K), as was the detrimental impact of STING on cell growth/apoptosis (Fig. 4L; Supplementary Fig. S4P). Together, these data identify cytosolic leakage of mtDNA as a key mediator of aberrant STING signaling and impaired cellular fitness in KL cells, conferring selection pressure to silence STING.

DISCUSSION

Here, we provide the first evidence that STING is actively suppressed following loss of the LKB1 tumor-suppressor gene. Whereas STING was previously reported to be eliminated by viral oncoproteins such as E1A and E7 (15), as a way for DNA tumor viruses to escape recognition, these findings uncover robust STING silencing in this major subset of *KRAS*-driven lung cancers. In contrast to its direct inactivation, suppression of STING expression in this context results from the combination of enhanced DNMT1 and EZH2 expression/activity, coupled with selection pressure to avoid the deleterious impact of mitochondrial stress and cytoplasmic mtDNA release. As a consequence, KL cells not only gain a cellular fitness advantage, but also lack PD-L1 expression

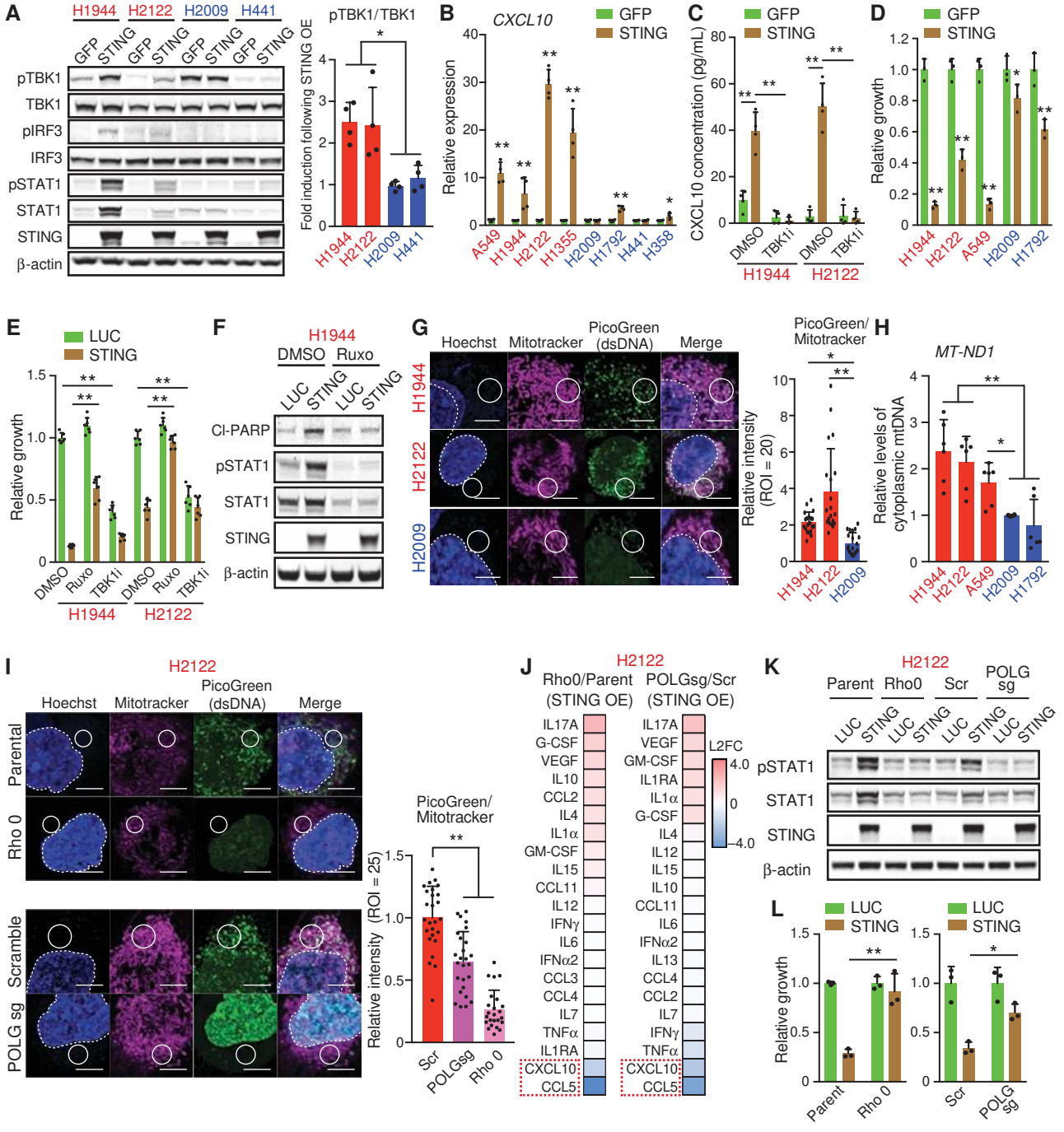

Figure 4. STING is poorly tolerated by *KRAS-LKB1*–mutant cells due to the pathologic accumulation of cytoplasmic dsDNA. **A** and **B,** IB of the indicated proteins (left) and quantification (right) of pTBK1 induction (**A**) or qRT-PCR of *CXCL10* (**B**) in KL (red) or KP (blue) cells 7 days following STING overexpression ($n = 4$ replicates from two independent experiments). **C,** CXCL10 ELISA in conditioned medium (CM) derived from KL cells 7 days following STING overexpression ± 1 μmol/L TBK1 inhibitor compound 1 for 72 hours. **D** and **E,** Relative cell number 9 days following STING overexpression ±1 μmol/L ruxo or 1 μmol/L TBK1 inhibitor Compound 1 ($n > 3$, biological replicates) following STING overexpression ($n = 4$, biological replicates). **F,** IB of the indicated proteins 7 days following STING reexpression ± 1 μmol/L ruxo treatment. **G,** H2009, H1944, or H2122 cells stained with PicoGreen, Mitotracker, and Hoechst (left). Scale bars, 3 μm. Signal intensity at each region of interest (ROI) was quantified by ImageJ (right). **H,** qPCR of mtDNA in cytoplasmic fraction ($n = 6$, biological replicates). **I,** Parental H2122, H2122 Rho 0, or H2122 cells transduced with scramble or *POLG* sgRNA stained with PicoGreen, Mitotracker, and Hoechst (left). Scale bars, 3 μm. Signal intensity at each ROI was quantified by ImageJ (right). **J,** Heat map of cytokine profiles in CM 7 days following STING reexpression. CMs were collected 72 hours after medium change. Scores, ratio of $\log_2$ fold change following STING reexpression relative to parental H2122 (left) or H2122 transduced with scramble sgRNA (right). **K,** IB of the indicated proteins 7 days following STING reexpression. **L,** Relative cell number 9 days following STING overexpression ($n = 3$, biological replicates). Values of STING-overexpressing cells were normalized to each control. *P* values were calculated by one-way (**A,G,H,** and **I**) or two-way (**B,C,D,E,** and **L**) ANOVA followed by Tukey *post hoc* test. *, $P < 0.05$; **, $P < 0.01$.

and downregulate chemokines that promote T-cell recruitment, providing important mechanistic insights into their lack of response to PD-1/PD-L1 ICB (3).

Following aberrant accumulation of cytoplasmic DNA derived from viral, bacterial, or other microbial pathogens, activation of STING promotes downstream effector TBK1-IRF3 pathway activation, producing type I IFNs and other STAT1-driven effector programs that are cytotoxic and designed to protect cells from these pathogenic states (8). In the absence of STING or activation of other viral sensors such as MAVS, TBK1 fails to bridge with IRF3 (16), favoring NF-κB–associated induction of alternate cytokines such as IL6 that instead promote cell survival and myeloid cell recruitment (1, 9). Indeed, TBK1- and IKKε-mediated protumorigenic cytokine circuits are known to contribute to tumor progression in *KRAS*-mutant lung cancers, involving IL6–STAT3 activation (9, 14). Importantly, epigenetic silencing of DNA sensing was restricted to STING expression, as KL cells maintained cGAS. Thus accumulation of upstream cGAMP, which can promote metastasis by extracellular transfer (17), could also contribute to LKB1-mutant tumor phenotypes.

STING is activated in certain cellular contexts that favor prosurvival signaling, such as aneuploid or endogenous retrovirus-expressing mesenchymal tumor cell subpopulations, resulting in preferential secretion of metastasis and tumor-promoting cytokines/chemokines (18, 19). Our data suggest that reactivation of STING in specific genomic contexts such as the KL cellular state shifts prosurvival TBK1 signaling toward this antiviral IRF3- and STAT1-driven program that promotes cell death. Thus, as an alternative to developing combination therapies that target *KRAS/LKB1*-mutant downstream signaling pathways (14), therapies that reinduce STING expression/signaling and preferentially engage this cytotoxic program in KL cells could be at least as effective.

Although recent advances in cancer immunotherapy via ICB have been dramatic, most patients fail to derive benefit, including those with *KRAS-LKB1* mutation (3). We also found that LKB1 and STING reinduction restored PD-L1 cell surface levels and induced the expression of CXCL10, which promotes T-cell chemotaxis. Thus, in addition to the negative cell-autonomous consequences that KL-mutant cancer cells endure upon STING reexpression, they also must defend themselves from T-cell recruitment by engaging the PD-1/PD-L1 immune checkpoint. Our data also therefore suggest that designing approaches to derepress STING in KL cells could sensitize these tumors to ICB. STING silencing was also associated with *LKB1* loss in *KRAS* WT lung cancers, and especially robust when combined with elevated DNMT1 levels, suggesting that this mechanism is not purely limited to the KL cellular state. Thus, low levels of tumor cell STING expression could be a promising general biomarker for intrinsic resistance to ICB. Developing strategies to reinduce its expression may thus prime antiviral and immune responses in additional genomic contexts and cancer subtypes.

Although our data also suggest that epigenetic reprogramming via treatment with DNMT1 and/or EZH2 inhibitors is one strategy to restore STING expression, it is possible that additional chromatin-modifying enzymes are involved and could represent viable therapeutic targets. Moreover, although we identified a dominant role for transcriptionally mediated STING repression, STING levels are also regulated by autophagy and endoplasmic reticulum stress (20, 21), and combination therapies that target these pathways and enhance STING expression posttranslationally may further exploit this vulnerability. Finally, our results also indicate that emerging strategies utilizing STING agonists or DNA-damaging agents to activate the STING pathway would be less effective in KL tumors, but could be particularly effective in combination with epigenetic and other therapies that increase STING levels. Given the need to retain STING agonists in the tumor bed and to penetrate the cancer cell membrane, liposomal delivery, antibody–STING agonist conjugates (22), or other tumor-targeting approaches are likely to be significantly more effective than current STING agonists in this regard.

METHODS

Data Analysis

The level 3 RNA-sequencing V2 datasets for lung adenocarcinoma samples were downloaded from the TCGA data portal and classified into KP samples ($n = 21$) or KL samples ($n = 17$) according to their mutation status (see Supplementary Table S1). Samples having mutations in both *LKB1* and *TP53* were excluded. TCGA IDs TCGA-78-7160, TCGA-78-7166, and TCGA-78-7540 were further eliminated because they were previously identified as a different subtype from KP or KL (23). *KRAS*-mutant lung adenocarcinoma cell lines in the CCLE repository were subdivided into two classes: KP ($n = 9$, H2009, H358, H1792, CALU6, H441, RERFLCAD2, HCC2108, HCC1171, and H2291) harboring a *KRAS* and *TP53* mutation/deletion with intact *LKB1*, and KL ($n = 9$, HCC44, H647, H2122, H1573, H1355, A549, H2030, H23, and H1944) harboring a *KRAS* and *LKB1* mutation, respectively. The RPKM values for each cell line were obtained from the CCLE repository. Then differentially expressed genes between KP and KL in CCLE and TCGA ($P < 0.05$ and FDR $q < 0.25$) were identified using the R platform and TCC package (24). Overlapped upregulated (59 genes) or downregulated (82 genes) genes in KL between CCLE and TCGA were extracted (see Supplementary Table S2) and then analyzed by GSEA with Reactome and Kyoto Encyclopedia of Genes and Genomes (KEGG) signatures. *KRAS* WT lung adenocarcinoma cell lines in the CCLE repository were also classified into *LKB1* WT and mutant (see Supplementary Table S3). CpG methylation levels of *STING* locus for each cell line were obtained from the CCLE repository.

IHC Staining and Analysis

Patients with *KRAS*-mutant NSCLC were identified through the DFCI PROFILE database. All patients were consented to an Institutional Review Board–approved research protocol allowing specimen collection and clinical data. Written informed consent was obtained from each patient, and studies were conducted in accordance with recognized ethical guidelines. Four-micron-thick formalin-fixed, paraffin-embedded tissue sections were stained at the Brigham & Women's Hospital Pathology Core. Staining for the following antibodies was performed on BOND-III, the fully automated IHC and ISH stainer (Leica Biosystems): anti-LKB1 (mouse, clone Ley 37d/g6, Abcam, Cat.# ab15095, EDTA-based pH 9.0 retrieval, dilution 1:1,500), anti-STING (rabbit, clone D2P2F, CST, Cat.# 13647, Citrate based pH 6.0 retrieval, dilution 1:500), anti-PD-L1 (rabbit, clone E1L3N, Cell Signaling Technology, Cat.# 13684, EDTA-based pH 9.0 retrieval, dilution 1:200), anti-CD3 (rabbit polyclonal, Dako, Cat.# A0452, EDTA-based pH 9.0 retrieval, dilution 1:250), anti-CD4 (mouse, clone 4B12, Dako, Cat.# M7310, EDTA-based pH 9.0 retrieval, dilution 1:250), and anti-CD8 (mouse, clone C8/144B, Dako, Cat.# M7103, EDTA-based pH 9.0 retrieval, dilution 1:100). Poly-HRP IgG reagent from Bond Polymer

Refine Detection Kit DC9800 was used to bind mouse and rabbit antibody. Sections were detected with DAB and counterstained with hematoxylin. LKB1 and STING stainings were visually scored by a pathologist for the assessment of LKB1 status and STING intensity in a majority of tumor cells. CD3, CD4, CD8, and PD-L1 quantification was performed by PathAI Inc. (https://www.pathai.com/) on Aperio-scanned images. Deep learning image analysis framework developed by PathAI was applied on the set of KRAS-mutant cases. The method consisted of the following stages: ground-truth annotation, deep learning model training for region-of-interest classification, and quantification of proportion of positive staining within each tissue region. To obtain ground-truth labels for the region of interest classifier, a pathologist annotated regions of cancer epithelium, cancer stroma, necrosis, and normal lung on a subset of study images. To provide ground-truth annotation for the IHC stain detection, a pathologist estimated amount of stain positivity in each tissue region for a subset of images. The PathAI system was applied to quantify CD3, CD4, and CD8 expression in the lung cancer epithelium and lung cancer stroma on all study images. The CD3, CD4, and CD8 T-cell tumor infiltration ratios were calculated by dividing the proportion of positive T-cell stain in regions of tumor epithelium by the proportion of positive T-cell stain in regions of stroma in each study image, using PathAI's stain quantification system.

Cell Lines

A549, A427, H2009, and HEK293T cells were cultured in DMEM (Thermo Fisher Scientific, Cat.# 11965-118) supplemented with 10% FBS (Gemini Bio-products, Cat.# 100-106), 1× penicillin–streptomycin (Gemini Bio-products, Cat.# 400-109), and 2.5 μg/mL plasmocin prophylactic (InvivoGen, Cat.# ant-mpp). H1944, H23, H1355, H2122, H1792, H441, H358, H1395, H838, H1437, H1755, H2228, H3255, H2087, H1793, H1650, and Jurkat cells were cultured in RPMI-1640 (Thermo Fisher Scientific, Cat.# 11875-119) supplemented with 10% FBS, 1× penicillin–streptomycin, and 2.5 μg/mL plasmocin prophylactic (InvivoGen, Cat.# ant-mpp). A549, A427, H1944, H23, H1355, H2122, H1792, and H2009 cells were originally obtained from the Broad Institute and authenticated by short tandem repeat genotyping. HEK293T, H441, H358, H1395, H838, H1437, H1755, H2228, H3255, H2087, H1793, and H1650 were purchased from the ATCC. All experiments were performed before reaching 10 passages. *Mycoplasma* infection was regularly checked by PCR using the conditioned media derived from each cell line. The sequences of the primers used for checking *Mycoplasma* infection are listed in Supplementary Table S4.

Immunoblotting

Cells were lysed in RIPA buffer containing 1× protease inhibitors (Roche, Cat.# 11-836-145-001) and phosphatase inhibitors (50 mmol/L NaF and 100 mmol/L Na_3VO_4). Immunoblotting was performed as described (14) using following antibodies: STING (#13647, Cell Signaling Technology), LKB1 (#3047, Cell Signaling Technology), phospho-AMPK (#2535, Cell Signaling Technology), AMPK (#5831, Cell Signaling Technology), DNMT1 (#5032, Cell Signaling Technology), EZH2 (#5246, Cell Signaling Technology), KDM5A (#A300-897A, Bethyl Laboratories), phospho-TBK1 (#5483, Cell Signaling Technology), TBK1 (#3013, Cell Signaling Technology), phospho-IRF3 (#4947, Cell Signaling Technology), IRF3 (#11904, Cell Signaling Technology), phospho-STAT1 (#9167, Cell Signaling Technology), STAT1 (#9172, Cell Signaling Technology), p62 (#5114, Cell Signaling Technology), NRF2 (#ab62352, Abcam), PARP (#9532, Cell Signaling Technology), cleaved PARP (#5625, Cell Signaling Technology), POLG (#13609, Cell Signaling Technology), and β-actin (#3700, Cell Signaling Technology). Secondary antibodies were from LI-COR Biosciences: IRDye 680LT Goat anti-Mouse IgG (#926-68020) and IRDye 800CW Goat anti-Rabbit IgG (#926-32211). Imaging of blots and quantitation of bands was performed using the LI-COR Odyssey system.

Quantitative RT-PCR

RNA extraction was performed using the RNeasy Mini Kit (Qiagen, Cat.# 74106). RNA samples (1 μg) were reverse-transcribed using SuperScript III First-Strand Synthesis SuperMix (Thermo Fisher Scientific, Cat.# 1683483). Quantitative real-time PCR was performed using Power SYBR Green PCR Master Mix (Thermo Fisher Scientific, Cat.# 4367659). The sequences of the primers used for qRT-PCR are listed in Supplementary Table S4. Values represent the average of four technical replicates from at least two independent experiments (biological replicates).

CRISPR/Cas9 System

Target sequences for CRISPR interference were designed using the single-guide RNA (sgRNA) designer (http://portals.broadinstitute.org/gpp/public/analysis-tools/sgrna-design). A nontargeting sgRNA from the Gecko library v2 was used as a scramble sgRNA. sgRNA target sequences are listed in Supplementary Table S4.

Generation of Lentivirus

HEK293T cells (3×10^6) were plated onto a 60-mm dish and transfected using X-tremeGENE HP DNA Transfection Reagent (Roche, Cat.# 06366236001) with 1 μg of lentivirus-based expression vectors together with 1 μg of pCMV-dR8.91 and 1 μg of pCMV-VSV-G. After 48-hour incubation, the media containing lentivirus particles were collected, passed through a 0.45 μm filter, and concentrated using Lenti-X Concentrator (Clontech, Cat.# 631231). For selection of virally infected cells, 0.5 to 2 μg/mL of puromycin (pCRISPR-v2 sgRNAs) or 1.5 to 8 μg/mL of blasticidin (plx304-GFP, plx304-NanoLuc, plx304-hLKB1-V5, plx304-hLKB1 kinase dead, plx304-hCXCR3, or plx304-hSTING) was used 24 hours after infection.

Reagents

The following reagents were used: MG-132 (Merck Millipore, Cat.# 474790), Bafilomycin A1 (Sigma-Aldrich, Cat.# B1793), phenformin hydrochloride (Cayman Chemical, Cat.# 14997), compound C (Merck Millipore, Cat.# 171260), DAC (Selleckchem, Cat.# S1200), GSK126 (Selleckchem, Cat.# S7061), KDM5-C70 (Xcessbio, Cat.# M60192), UNC0638 (Tocris, Cat.# 4343), ADU-S100 (Chemietek, Cat.# CT-ADUS100), and ruxolitinib (Selleckchem, Cat.# S1378). TBK1 inhibitor compound 1 was supplied by Gilead Sciences, Inc.

Methylated DNA Immunoprecipitation

DNA extraction was performed using the QIAamp DNA Mini Kit (Qiagen, Cat. #51304) according to the manufacturer's instructions. Next, 4 μg of genomic DNA in 1 mL of low TE was sonicated with Covaris LE220. Quality of DNA sharing was analyzed by High Sensitivity DNA Chips (Agilent Technologies, Cat.# 5067-4626) according to the manufacturer's instructions (the range of DNA fragment is 200 to 500 bp). Methylated DNA immunoprecipitation was performed using monoclonal antibody against 5-mc33D3 (Diagenode, Cat.# C15200081) labeled with magnetic Dynabeads anti-mouse IgG (Invitrogen, Cat.# M-280). Sheared DNA and antibody coupled to the magnetic beads were incubated overnight at 4°C. DNA combined with beads was washed 6 times with immunoprecipitation wash buffer [2 mmol/L EDTA, 20 mmol/L Tris-HCl (pH 8.0), 0.1% SDS, 150 mmol/L NaCl, 1% Triton X-100], and DNA was eluted from the beads in digestion buffer [10 mmol/L EDTA, 10 mmol/L Tris-HCl (pH 8.0), 0.5% SDS, 50 mmol/L NaCl] with proteinase K at 50°C for 30 minutes. Ten percent input DNA was used as control. The sequences of the primers used for chromatin immunoprecipitation (ChIP) qPCR (400–550 bp downstream from the *STING* transcription start site (TSS), NM_198282.3) are listed in Supplementary Table S4.

ChIP

Cells (1×10^7) were cross-linked by 1% paraformaldehyde in fixing buffer (50 mmol/L HEPES, pH 7.5, 100 mmol/L NaCl, 1 mmol/L

EDTA, pH 8.0) for 5 minutes at room temperature, and then the cross-linking reaction was quenched by the addition of 1.25 mol/L glycine. Cells were washed once with cold PBS, collected into tubes by centrifugation, washed once with cold PBS again, and then resuspended in lysis buffer (140 mmol/L NaCl, 50 mmol/L HEPES, pH 8.0, 1 mmol/L EDTA, pH 8.0, 10% glycerol, 0.5% NP-40, 0.25% Triton X-100, 1 x protease inhibitor, and 1 x phosphatase inhibitor). The subsequent cell pellet was washed with wash buffer (200 mmol/L NaCl, 10 mmol/L Tris-HCl, pH 8.0, 1 mmol/L EDTA pH 8.0, 1 x protease inhibitor, and 1 x phosphatase inhibitor), resuspended in 1 mL shearing buffer (0.1% SDS, 10 mmol/L Tris-HCl, pH 8.0, 1 mmol/L EDTA, pH 8.0, 1 x protease inhibitor, 1 x phosphatase inhibitor) and sonicated with Covaris LE220. After DNA shearing, 110 μL 10% Triton X-100 and 33 μL 5 mol/L NaCl were added to 1 mL sonicated lysates. Then lysates were incubated with 5 μg rabbit anti-histone H3K27me3 antibody (Abcam, Cat.# ab6002) or anti-DNMT1 antibody (Abcam, Cat.# ab13537) overnight at 4°C, and then incubated with 20 μL PureProteome Protein G Magnetic Beads (Millipore, Cat.# LSKMAGG02) for 2 hours at 4°C. Beads were washed once with low salt immune complex buffer (150 mmol/L NaCl, 0.1% SDS, 20 mmol/L Tris-HCl, pH 8.0, 1% Triton X-100, 2 mmol/L EDTA, pH 8.0), high salt immune complex buffer (500 mmol/L NaCl, 0.1% SDS, 20 mmol/L Tris-HCl, pH 8.0, 1% Triton X-100, 2 mmol/L EDTA, pH 8.0), LiCl immune complex buffer (250 mmol/L LiCl, 10 mmol/L Tris-HCl, pH 8.0, 1% NP-40, 1% sodium deoxycholate, 1 mmol/L EDTA, pH 8.0), and then TE buffer. Cross-links were reversed overnight at 65°C. RNA and protein were digested using 200 μg/mL RNase A (Thermo Fisher Scientific, Cat.# EN0531) and 200 μg/mL Proteinase K (Thermo Fisher Scientific, Cat.# EO0491) respectively, and DNA was purified with phenol chloroform extraction and ethanol precipitation. Quality of DNA sharing was analyzed by High Sensitivity DNA Chips (Agilent Technologies; Cat.# 5067-4626) according to the manufacturer's instructions. Total amount of ChIPed DNA was analyzed by Qubit dsDNA HS assay kit (Thermo Fisher Scientific; Cat.# Q32851) according to the manufacturer's instructions. The sequences of the primers used for ChIP-qPCR (400–550 bp downstream from the *STING* TSS, NM_198282.3) are listed in Supplementary Table S4.

SAM Fluorescence Assay

The amount of S-adenosylmethionine was measured using the Bridge-IT SAM fluorescence Kit (Mediomics, Cat.# 1-1-10038) according to the manufacturer's instructions.

dsDNA or dsRNA Stimulation

Cells (2 to 5×10^5) were plated onto a 6-well plate and transfected using X-tremeGENE HP DNA Transfection Reagent (Roche, Cat.# 06366236001) with the indicated amount of poly (dA:dT) (InvivoGen, Cat.# tlrl-patn) or poly (I:C) (InvivoGen, Cat.# tlrl-pic).

ELISA

Human IFNβ (Thermo Fisher Scientific, Cat.# 414101), CXCL10 (R&D systems, Cat.# DIP100), and CCL5 (R&D systems, Cat.# DRN00B) ELISAs were performed according to the manufacturer's instructions. Conditioned media from each cell lines were collected after 24- or 72-hour culture. Values represent the average of four replicates from at least two independent experiments (biological replicates).

Cytokine Profiling

Multiplex assays were performed utilizing the bead-based immunoassay approach Bio-Plex Pro Human Cytokine 40-plex Assay (Cat.# 171AK99MR2) on a Bio-Plex 200 system (Bio-Rad Laboratories, Cat.# 171000201) and the Human Cytokine/Chemokine Magnetic Bead Panel (Cat.# HCYTMAG-60K-PX30) on a Luminex MAGPIX system (Merck Millipore). Conditioned media concentration levels (pg/mL) of each protein were derived from 5-parameter curve fitting models. Fold changes relative to the corresponding control were calculated and plotted as log2FC. Lower and upper limits of quantitation (LLOQ/ULOQ) were imputed from standard curves for cytokines above or below detection.

Cell Viability Assay

A549 cells were cultured in the presence of 100 nmol/L DAC for 7 days for pretreatment. Three thousand cells were plated onto 96-well plates, stimulated by the indicated amount of poly (dA:dT), and then incubated for 96 hours. Values of CellTiter-Glo Luminescent Cell Viability assay (Promega) after 96 hours were normalized to vehicle-treated cells. Plates were read on a Tecan Infinite M200 Pro plate reader, and analysis was performed using Prism7 (GraphPad Software). All conditions were tested in triplicate.

Infiltration Assay

Cancer cell spheroids were generated by seeding 5×10^5 cells in suspension in an ultra-low attachment dish (Corning, Cat.# 3471) for 24 hours. Samples were pelleted and then resuspended in type I rat tail collagen (Corning) at a concentration of 2.5 mg/mL following the addition of 10 × PBS with phenol red with pH adjusted using NaOH. pH of 7.0 to 7.5 was confirmed using PANPEHA Whatman paper (Sigma-Aldrich). The spheroids-collagen suspension was then injected into the central gel region of the DAX-1 3-D microfluidic cell culture chip (AIM Biotech, Singapore, Cat.# DAX-1). Microfluidic devices were designed as previously described (10), with a central region containing the cell–collagen mixture in a 3-D microenvironment, surrounded by two media channels located on either side. After injection, collagen hydrogels containing cells were incubated for 40 minutes at 37°C in humidity chambers, then hydrated with RPMI culture media, with or without 2.5×10^4 CXCR3-overexpressing Jurkat cells and in one of the side media channels. CXCR3-overexpressing Jurkat cells were labeled with Cell Tracker Red (Thermo Fisher Scientific, Cat.# C34552) following the manufacturer's instructions. After 72 to 96 hours of incubation, cancer cell spheroids and infiltrated Jurkat cells were rinsed twice in PBS and fixed in 4% paraformaldehyde (Electron Microscopy Sciences, Cat.# 15700) for 15 minutes at room temperature. Cell membranes were permeabilized with 0.1% vol/vol Triton X-100 (Sigma-Aldrich, Cat.# X100-500ML) for 5 minutes at room temperature (RT) and washed twice in PBS. After blocking with 1% BSA (Sigma-Aldrich, Cat.# A4503-100G) in PBS overnight at 4°C, devices were stained by conjugated Alexa Fluor 647 anti-human CD326 (EPCAM) Antibody (BioLegend, Cat.# 324212; 1:100, volume ratio) and placed on a shaker at RT for 3 to 4 hours. After PBS washing, devices were imaged using a confocal laser scanning microscope (FMV-1000, Olympus). For quantification, images were captured on a Nikon Eclipse 80i fluorescence microscope equipped with Z-stack (Prior) and CoolSNAP CCD camera (Roper Scientific). Image capture and analysis was performed using NIS-Elements AR software package. Whole device images were achieved by stitching in multiple captures. Quantification of cell infiltration into the 3-D tumor microenvironment was performed by measuring the total cell area of cell tracker dye in the entire gel region.

Flow Cytometry

Cells (1×10^6) resuspended in 100 μL PBS containing 3% FBS were stained by PE/Cy7-conjugated anti–PD-L1 antibody (BioLegend, Cat.# 329718) for 30 minutes at room temperature, washed by PBS containing 3% FBS, and then analyzed by FACSCanto II (BD Biosciences). PE/Cy7-conjugated mouse IgG2b (BioLegend, Cat.# 400325) was used as isotype control antibody. For apoptosis analysis, cells were stained by Annexin V using Alexa Fluor 488

Annexin V dead cell apoptosis kit (Thermo Fisher Scientific, Cat.# V13245) according to the manufacturer's instructions and then analyzed by FACSCanto ll (BD Biosciences).

Animal Study

Eight-week-old SHO mice (SCID Hairless Outbred; Charles River Laboratories) were used in this study. Mouse experiments were conducted in accordance with a Dana-Farber Cancer Institute Institutional Animal Care and Use Committee–approved protocol. A549 cells were pretreated with 100 nmol/L DAC for 7 days and stimulated at 80% confluence by 5 μg poly (dA:dT) on the D150 plate. Twenty-four hours after stimulation by poly (dA:dT), live cells were counted prior to implantation and resuspended in RPMI-1640: Matrigel (1:1); 5×10^6 cells in 200 μL media were injected subcutaneously per mouse. Tumor growth was monitored every day or every other day after implantation, and when tumor size was measurable (day 7), the tumors were measured with a digital caliper twice a week.

Isolation of Cytoplasmic dsDNA

Cytoplasmic DNA was extracted by using mitochondrial DNA isolation kit (BioVision, Cat.# K280-50) according to modified manufacturer's instructions. In brief, 5×10^6 cells were lysed with cytosol extraction buffer, homogenized by dounce tissue grinder (40 times), and then the nuclei and mitochondrial fractions were removed by centrifugation according to the manufacturer's instructions. Cytoplasmic DNA was purified by RNase A (Thermo Fisher Scientific, Cat.# EN0531) and Proteinase K (Thermo Fisher Scientific, Cat.# EO0491) treatment, phenol/chloroform extraction, and ethanol precipitation with a carrier (Dr. GenTLE Precipitation Carrier, Takara Bio, Cat.# 9094). The amount of mtDNA in cytosol was determined by qPCR using MT-ND1 primers. The amount of nuclear DNA in cytosol was determined by qPCR using three different sets of primers designed for different chromosomes as described previously (25). The sequences of the primers are listed in Supplementary Table S4.

Statistical Analysis

Statistical significance was assessed using unpaired two-tailed Student *t* test, one-way ANOVA followed by Tukey *post hoc* test, or two-way ANOVA followed by Tukey *post hoc* test. *P* values less than 0.05 were considered significant. Asterisks used to indicate significance correspond with *, $P < 0.05$ and **, $P < 0.01$. Columns represent means ± SD. In one-way or two-way ANOVA followed by *post hoc* tests, we showed asterisks only in pairs of our interest. GraphPad Prism7 was used for all statistical analysis.

Disclosure of Potential Conflicts of Interest

C.P. Paweletz has received honoraria from the speakers bureaus of Bio-Rad and AstraZeneca Korea, and is a consultant/advisory board member for DropWorks. D.A. Barbie reports receiving commercial research grants from Bristol-Myers Squibb and Novartis; has received honoraria from the speakers bureaus of Loxo Oncology and Madalon Consulting; and is a consultant/advisory board member for N of One. No potential conflicts of interest were disclosed by the other authors.

Authors' Contributions

Conception and design: S. Kitajima, M. Yajima, D.A. Barbie
Development of methodology: S. Kitajima, S. Guo, R. Yoshida, M. Yajima, D.A. Barbie
Acquisition of data (provided animals, acquired and managed patients, provided facilities, etc.): S. Kitajima, E. Ivanova, S. Guo, R. Yoshida, M. Campisi, S.K. Sundararaman, T.C. Thai, S. Masuda, B.P. Piel, L.M. Sholl, C.P. Paweletz, H. Watanabe, M. Yajima
Analysis and interpretation of data (e.g., statistical analysis, biostatistics, computational analysis): S. Kitajima, E. Ivanova, M. Campisi, S.K. Sundararaman, S. Tange, Y. Mitsuishi, B.P. Piel, H. Watanabe, M. Yajima
Writing, review, and/or revision of the manuscript: S. Kitajima, E. Ivanova, M. Campisi, Y. Mitsuishi, L.M. Sholl, C.P. Paweletz, H. Watanabe, D.A. Barbie
Administrative, technical, or material support (i.e., reporting or organizing data, constructing databases): Y. Mitsuishi, B.P. Piel, P.T. Kirschmeier
Study supervision: Y. Mitsuishi, P.T. Kirschmeier, D.A. Barbie

Acknowledgments

This work was supported by NCI-R01 CA190394-02 and NIH-U01 CA2143A1-01 (D.A. Barbie), the Gloria T. Maheu, Heerwagen, Candice Bagby, and Gross-Loh Family Funds for Lung Cancer Research (D.A. Barbie), and the JSPS Postdoctoral Fellowship for Research Abroad (S. Kitajima). Research was also supported by a Stand Up To Cancer-American Cancer Society Lung Cancer Dream Team Translational Research Grant (SU2C-AACR-DT17-15; D.A. Barbie). Stand Up To Cancer (SU2C) is a division of the Entertainment Industry Foundation. Research grants are administered by the American Association for Cancer Research, the Scientific Partner of SU2C.

The costs of publication of this article were defrayed in part by the payment of page charges. This article must therefore be hereby marked *advertisement* in accordance with 18 U.S.C. Section 1734 solely to indicate this fact.

Received June 15, 2018; revised September 21, 2018; accepted October 3, 2018; published first October 8, 2018.

REFERENCES

1. Koyama S, Akbay EA, Li YY, Aref AR, Skoulidis F, Herter-Sprie GS, et al. STK11/LKB1 deficiency promotes neutrophil recruitment and proinflammatory cytokine production to suppress T-cell activity in the lung tumor microenvironment. Cancer Res 2016;76:999–1008.
2. Kitajima S, Thummalapalli R, Barbie DA. Inflammation as a driver and vulnerability of KRAS mediated oncogenesis. Semin Cell Dev Biol 2016;58:127–35.
3. Skoulidis F, Goldberg ME, Greenawalt DM, Hellmann MD, Awad MM, Gainor JF, et al. STK11/LKB1 mutations and PD-1 inhibitor resistance in KRAS-mutant lung adenocarcinoma. Cancer Discov 2018;8:822–35.
4. Egan DF, Shackelford DB, Mihaylova MM, Gelino S, Kohnz RA, Mair W, et al. Phosphorylation of ULK1 (hATG1) by AMP-activated protein kinase connects energy sensing to mitophagy. Science 2011;331:456–61.
5. Shackelford DB, Abt E, Gerken L, Vasquez DS, Seki A, Leblanc M, et al. LKB1 inactivation dictates therapeutic response of non-small cell lung cancer to the metabolism drug phenformin. Cancer Cell 2013;23:143–58.
6. Kottakis F, Nicolay BN, Roumane A, Karnik R, Gu H, Nagle JM, et al. LKB1 loss links serine metabolism to DNA methylation and tumorigenesis. Nature 2016;539:390–5.
7. Wan L, Xu K, Wei Y, Zhang J, Han T, Fry C, et al. Phosphorylation of EZH2 by AMPK suppresses PRC2 methyltransferase activity and oncogenic function. Mol Cell 2018;69:279–91e5.
8. Barber GN. STING: infection, inflammation and cancer. Nat Rev Immunol 2015;15:760–70.
9. Zhu Z, Aref AR, Cohoon TJ, Barbie TU, Imamura Y, Yang S, et al. Inhibition of KRAS-driven tumorigenicity by interruption of an autocrine cytokine circuit. Cancer Discov 2014;4:452–65.
10. Jenkins RW, Aref AR, Lizotte PH, Ivanova E, Stinson S, Zhou CW, et al. Ex vivo profiling of PD-1 blockade using organotypic tumor spheroids. Cancer Discov 2018;8:196–215.

11. McArthur K, Whitehead LW, Heddleston JM, Li L, Padman BS, Oorschot V, et al. BAK/BAX macropores facilitate mitochondrial herniation and mtDNA efflux during apoptosis. Science 2018;359.
12. Xia T, Konno H, Barber GN. Recurrent Loss of STING signaling in melanoma correlates with susceptibility to viral oncolysis. Cancer Res 2016;76:6747–59.
13. Garcia-Diaz A, Shin DS, Moreno BH, Saco J, Escuin-Ordinas H, Rodriguez GA, et al. Interferon receptor signaling pathways regulating PD-L1 and PD-L2 expression. Cell Rep 2017;19:1189–201.
14. Kitajima S, Asahina H, Chen T, Guo S, Quiceno LG, Cavanaugh JD, et al. Overcoming resistance to dual innate immune and MEK inhibition downstream of KRAS. Cancer Cell 2018;34:439–52e6.
15. Lau L, Gray EE, Brunette RL, Stetson DB. DNA tumor virus oncogenes antagonize the cGAS-STING DNA-sensing pathway. Science 2015;350:568–71.
16. Liu S, Cai X, Wu J, Cong Q, Chen X, Li T, et al. Phosphorylation of innate immune adaptor proteins MAVS, STING, and TRIF induces IRF3 activation. Science 2015;347:aaa2630.
17. Chen Q, Boire A, Jin X, Valiente M, Er EE, Lopez-Soto A, et al. Carcinoma-astrocyte gap junctions promote brain metastasis by cGAMP transfer. Nature 2016;533:493–8.
18. Canadas I, Thummalapalli R, Kim JW, Kitajima S, Jenkins RW, Christensen CL, et al. Tumor innate immunity primed by specific interferon-stimulated endogenous retroviruses. Nat Med 2018;24:1143–50.
19. Bakhoum SF, Ngo B, Laughney AM, Cavallo JA, Murphy CJ, Ly P, et al. Chromosomal instability drives metastasis through a cytosolic DNA response. Nature 2018;553:467–72.
20. Terai H, Kitajima S, Potter DS, Matsui Y, Quiceno LG, Chen T, et al. ER stress signaling promotes the survival of cancer "persister cells" tolerant to EGFR tyrosine kinase inhibitors. Cancer Res 2018;78:1044–57.
21. Konno H, Konno K, Barber GN. Cyclic dinucleotides trigger ULK1 (ATG1) phosphorylation of STING to prevent sustained innate immune signaling. Cell 2013;155:688–98.
22. STINGing antitumor immunity into action. Cancer Discov 2018;8:259–60.
23. Skoulidis F, Byers LA, Diao L, Papadimitrakopoulou VA, Tong P, Izzo J, et al. Co-occurring genomic alterations define major subsets of KRAS-mutant lung adenocarcinoma with distinct biology, immune profiles, and therapeutic vulnerabilities. Cancer Discov 2015;5:860–77.
24. Sun J, Nishiyama T, Shimizu K, Kadota K. TCC: an R package for comparing tag count data with robust normalization strategies. BMC Bioinformatics 2013;14:219.
25. Takahashi A, Loo TM, Okada R, Kamachi F, Watanabe Y, Wakita M, et al. Downregulation of cytoplasmic DNases is implicated in cytoplasmic DNA accumulation and SASP in senescent cells. Nat Commun 2018;9:1249.